

## Evaluating Simulated Microphysics during OLYMPEX Using GPM Satellite Observations

ROBERT CONRICK AND CLIFFORD F. MASS

*Department of Atmospheric Sciences, University of Washington, Seattle, Washington*

(Manuscript received 5 September 2018, in final form 28 January 2019)

### ABSTRACT

This study evaluates moist physics in the Weather Research and Forecasting (WRF) Model using observations collected during the Olympic Mountains Experiment (OLYMPEX) field campaign by the Global Precipitation Measurement (GPM) satellite, including data from the GPM Microwave Imager (GMI) and Dual-Frequency Precipitation Radar (DPR) instruments. Even though WRF using Thompson et al. microphysics was able to realistically simulate water vapor concentrations approaching the barrier, there was underprediction of cloud water content and rain rates offshore and over western slopes of terrain. We showed that underprediction of rain rate occurred when cloud water was underpredicted, establishing a connection between cloud water and rain-rate deficits. Evaluations of vertical hydrometeor mixing ratio profiles indicated that WRF produced too little cloud water and rainwater content, particularly below 2.5 km, with excessive snow above this altitude. Simulated mixing ratio profiles were less influenced by coastal proximity or mid-latitude storm sector than were GMI profiles. Evaluations of different synoptic storm sectors suggested that postfrontal storm sectors were simulated most realistically, while warm sectors had the largest errors. DPR observations confirm the underprediction of rain rates noted by GMI, with no dependence on whether rain occurs over land or water. Finally, WRF underpredicted radar reflectivity below 2 km and overpredicted above 2 km, consistent with GMI vertical mixing ratio profiles.

### 1. Introduction

The evaluation of mesoscale weather prediction models over coastal mountains is of substantial importance because orographically forced coastal precipitation is critical for the water resources that serve many highly populated areas (Barros 2013). The properties of coastal precipitation systems depend on the upstream environment over the ocean, where collecting observations is difficult (Stoelinga et al. 2013). As a result, satellite-derived measurements are often the sole source of observations for evaluating simulated moist physics over coastal and offshore areas. Furthermore, continuous sampling from satellite observing systems provides long-term datasets, which would otherwise be prohibitive to obtain.

A number of studies have used satellite observations to evaluate model moist physics, with some relying on infrared measurements—particularly cloud-top brightness temperature—to assess simulated cloud fields (e.g., Garand and Nadon 1998; Chaboureau et al. 2002;

Keil et al. 2003; Sun and Rikus 2004; Otkin and Greenwald 2008; Jankov et al. 2011). In one assessment using simulated cloud-top brightness temperatures, Jankov et al. (2011) found that several moist physics parameterizations underestimated midlevel clouds during atmospheric river events. Bikos et al. (2012) used brightness temperatures to show that simulations underestimated low-level cloud in a pre-convective environment.

Other satellite datasets used to evaluate simulated cloud properties and rainfall include those from the Tropical Rainfall Measurement Mission (TRMM; Kummerow et al. 1998), the Moderate Resolution Imaging Spectroradiometer (MODIS), and *CloudSat* (Stephens et al. 2002). Using MODIS observations of a midlatitude cyclone, Otkin and Greenwald (2008) demonstrated an overprediction of cloud depth over the North Atlantic in the Weather Research and Forecasting (WRF) Model. Bodas-Salcedo et al. (2012) used a variety of satellite datasets, including MODIS, to show that WRF produced insufficient low- and midlevel cloud over midlatitude oceanic regions, which was also demonstrated by Huang et al. (2014)

---

*Corresponding author:* Robert Conrick, rconrick@uw.edu

DOI: 10.1175/JAS-D-18-0271.1

© 2019 American Meteorological Society. For information regarding reuse of this content and general copyright information, consult the [AMS Copyright Policy](https://www.ametsoc.org/PUBSReuseLicenses) ([www.ametsoc.org/PUBSReuseLicenses](https://www.ametsoc.org/PUBSReuseLicenses)).

using the A-Train<sup>1</sup> constellation of satellites. In addition, several studies using satellite measurements found that NWP models favor low rain rates (e.g., Laviola et al. 2011) and underpredict heavy rainfall events (e.g., Rakesh et al. 2009; Vasić et al. 2007; Zhang et al. 2013; Kim et al. 2013). Relatively little work has focused on model evaluation using satellite-based radar reflectivity, although results from Shi et al. (2010), using *CloudSat* and the Advanced Microwave Sounding Unit, indicated that WRF produces larger values of simulated reflectivity than observed. The extent to which simulated rainfall errors are related to errors in cloud representation remains unclear, particularly offshore of coastal mountains.

To provide global coverage of three-dimensional cloud and precipitation distributions from a single platform, the National Aeronautics and Space Administration (NASA) Global Precipitation Measurement (GPM) satellite mission (Hou et al. 2014; Skofronick-Jackson et al. 2017) was launched in 2014. The GPM satellite contains two instruments for observing clouds and precipitation: the GPM Microwave Imager (GMI) and the Dual-Frequency Precipitation Radar (DPR), both of which are used in this study. To provide ground validation for the GPM satellite, the Olympic Mountains Experiment (OLYMPEX) was conducted during the winter of 2015/16 over the Olympic Peninsula of Washington State. In addition to the GPM satellite, the OLYMPEX campaign deployed aircraft, radar, and a suite of surface observing stations to sample a variety of midlatitude frontal systems (Houze et al. 2017).

This study uses GPM observations to evaluate cloud and precipitation fields from the WRF Model. Measurements from GPM provide a unique opportunity to elucidate possible deficiencies in simulated moist physics across a range of spatial and temporal scales. In particular, GPM data allow for the evaluation of moist physics upstream and over the Olympic Mountains. This paper expands on the work of Conrick and Mass (2018, manuscript submitted to *J. Hydrometeor.*), which used surface observations and WRF simulations to show that winter precipitation is underpredicted along the Pacific Northwest coastal zone despite realistic simulations of incoming integrated vapor transport (IVT). Specifically, this paper addresses the following questions:

1) How well does WRF simulate GPM-observed water vapor, cloud water, and rain rate during OLYMPEX?

- 2) Can the underprediction of precipitation over coastal regions, described in Conrick and Mass (2018, manuscript submitted to *J. Hydrometeor.*), be explained by upstream (offshore) GPM measurements? Can cloud water or water vapor fields explain precipitation biases?
- 3) How realistic are simulated vertical profiles of rainwater, cloud water, and snow mixing ratios compared to GPM observations? Are vertical profiles of simulated reflectivity consistent with observed hydrometeor profiles?
- 4) Do varying environmental conditions, such as those of different midlatitude storm sectors, influence model skill? Does the accuracy of simulated rain rate or reflectivity depend on surface type (ocean vs land)?

This paper is organized as follows: section 2 reviews GPM data and model configuration, section 3 describes results of our model evaluation using GPM, and section 4 offers concluding remarks.

## 2. Model configuration and GPM data

### a. Model configuration

During OLYMPEX, operational forecasts were produced at the University of Washington using the WRF (Skamarock et al. 2008) Model, version 3.7.1. As in Conrick and Mass (2018, manuscript submitted to *J. Hydrometeor.*), we use archived WRF forecasts, valid every 6 h from 0600 to 2400 UTC and initialized daily at 0000 UTC, for the period from 1 November 2015 to 1 February 2016. A 36–12–4–1.33-km domain configuration was utilized with 38 vertical levels, with the innermost domain encompassing all of Washington State and its nearshore waters (Fig. 1).

Lateral boundaries for WRF were updated and the 36-km grid was nudged every 3 h using 0.5° National Oceanic and Atmospheric Administration (NOAA)/National Weather Service Global Forecast System (GFS) gridded forecasts, which also served as model initialization conditions. Some surface parameters were initialized from other sources.<sup>2</sup> Model parameterization choices included the Noah LSM with multiparameterization options (Noah-MP; Niu et al. 2011), the Rapid Radiative Transfer Model for GCMs (RRTMG) radiation scheme (Iacono et al. 2008), and the Yonsei University (YSU; Hong et al. 2006)

<sup>1</sup>The NASA A-Train constellation of satellites consists of *OCO-2*, *GCOM-WI*, *Aqua*, *CALIPSO*, *CloudSat*, and *Aura*. More details can be found online (<https://atrain.nasa.gov/>).

<sup>2</sup>See the University of Washington online weather prediction portal for additional information (<https://atmos.washington.edu/wrfrft/>).

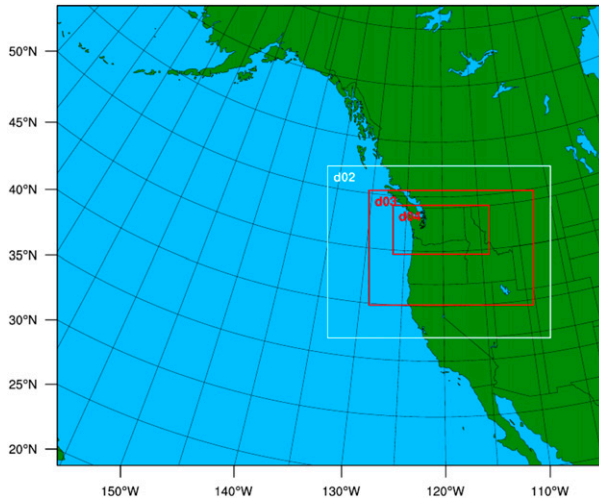


FIG. 1. The WRF-ARW domains used during OLYMPEX. Labels d02, d03, and d04 indicate domains with 12-, 4-, and 1.33-km grid spacing, respectively.

boundary/surface-layer scheme. A cumulus parameterization scheme (Grell–Freitas; Grell and Freitas 2014) was used in all but the 1.33-km domain. Only forecasts from the 1.33-km domain are considered in our analyses.

The Thompson microphysics parameterization (Thompson et al. 2008) is used by the University of Washington WRF and was employed for the OLYMPEX simulations. The Thompson scheme is a single-moment microphysical parameterization scheme that predicts the mass mixing ratios of five microphysical species: water vapor, cloud water, cloud ice, rainwater, snow, and graupel. For additional accuracy, rainwater and cloud ice number concentrations are predicted, thus making the scheme double moment for these quantities. The scheme assumes exponential size distributions for all species except cloud water ( $\gamma$ ) and snow [sum of  $\gamma$  and exponential following Field et al. (2005)].

### b. GPM data

Data from two GPM instruments were obtained from the NASA Goddard Earth Sciences Data and Information Services Center: the GMI (Wentz et al. 2015; Iguchi and Meneghini 2016a) and the Ku-band GPM DPR (Iguchi and Meneghini 2016b). Due to orbital configuration, the GPM satellite is capable of observing between 65°N and 65°S. We consider data from the OLYMPEX winter: 1 November 2015–1 February 2016, during which period there were 85 of 92 days where at least a portion of the GMI analysis domain in Fig. 2 was sampled.

The GPM GMI instrument collects data along a 904-km-wide swath with a 13-km horizontal resolution and 250-m vertical resolution. The operating

frequencies of GMI range from 10 to 183 GHz. Within the DPR instrument, the Ku-band radar operates at a frequency of 13.6 GHz, which is the same frequency as the successful TRMM Precipitation Radar. The GPM DPR Ku-band radar collects observations within a narrower (245 km) swath on a 5-km grid centered within the larger GMI overpass swath at 250-m vertical resolution. The DPR provides measurements over land as well as water, and thus western Washington and its nearshore Pacific waters can be analyzed simultaneously.

As described in the GPM Science Implementation Plan,<sup>3</sup> the random instrument errors of the GMI and DPR sensors were similar or better than microwave instruments aboard TRMM. The GMI bias met GPM mission requirements and was dependent on rain rate, decreasing from a bias of 0.25 mm h<sup>-1</sup> at rain rates of 1 mm h<sup>-1</sup> to 0.1 mm h<sup>-1</sup> at rates of 10 mm h<sup>-1</sup>, with a sensitivity of 0.2 mm h<sup>-1</sup>. The DPR instrument has an uncertainty range of  $\pm 1$  dB. We use the Ku-band retrievals from DPR because of its similarity to the successful TRMM Precipitation Radar and because it has been shown to be more accurate than DPR's Ka-band radar, which was found by Kubota et al. (2014) to underestimate precipitation.

While not necessarily generalizable to the OLYMPEX campaign due to differing topography and meteorology, a number of GPM evaluation studies have compared GPM observations to those of TRMM. Tian et al. (2018) demonstrated that GPM rain retrievals generally overestimated light rainfall events and underestimated heavy events over land. In spite of this, studies indicate that GPM is more accurate than TRMM when determining whether precipitation is occurring (Gao et al. 2017) and light precipitation rates over complex terrain (Ma et al. 2016). In one study over the Swiss Alps using surface radars and rain gauges, Speirs et al. (2017) showed that GPM retrievals generally underestimate precipitation during the winter, being most accurate when liquid-phase precipitation is occurring.

### c. GPM data and WRF output processing

Figure 2 shows our GMI analysis domain, which describes flow characteristics upstream of the Pacific Northwest coastal zone, while still remaining within our highest-resolution WRF domain. For each satellite overpass, we analyze daily mean column-integrated quantities of water vapor and cloud water content, and

<sup>3</sup> Appendixes A, D, and F of the GPM Science Implementation Plan (<https://pmm.nasa.gov/category/document-type/science-implementation-plans>) outline error requirements and information.

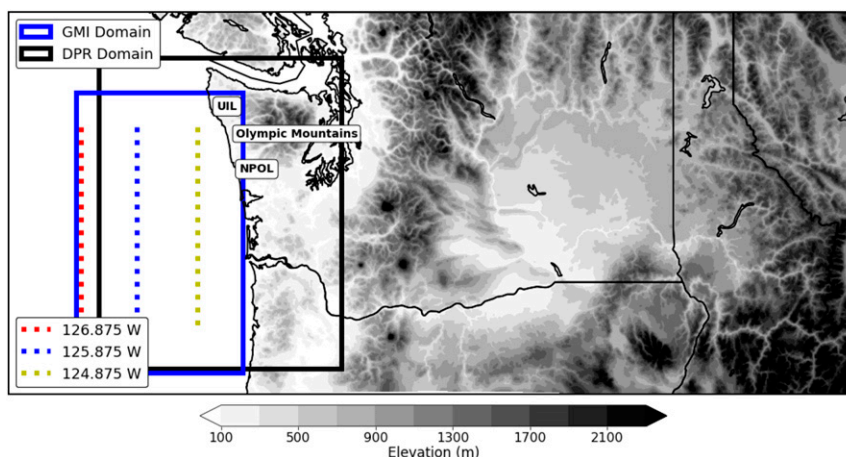


FIG. 2. The domains used for GPM GMI and DPR analyses, in the context of the 1.33-km WRF domain, with selected longitudes labeled (yellow:  $\sim 30$  km from the coast; blue:  $\sim 110$  km; and red:  $\sim 190$  km). The UIL rawinsonde location, the NPOL, and the Olympic Mountains are labeled, and elevation is shaded.

rain rate at the surface from Remote Sensing Systems (RSS),<sup>4</sup> with data interpolated to a  $0.25^\circ$  grid. Because GMI data are valid only over water due to microwave retrieval constraints, land areas are removed from GMI data along with points where adverse conditions occur, such as sun glare (Wentz et al. 2015). In addition, we obtain from NASA<sup>5</sup> daily mean vertical profiles of cloud water, rainwater content, and snow concentrations from the GMI instrument. For comparisons of GMI to the model, WRF output is analyzed on the same  $0.25^\circ$  grid over water. To produce a fair but comprehensive comparison, we remove data from both datasets where model or observed quantities are missing or null, as well as locations where WRF output are outside of the GMI swath. Thus, both datasets have the same sample sizes to facilitate statistical comparison. Daily mean vertical profiles are computed by RSS as the mean of the ascending and descending satellite passes on a given day. WRF daily means are computed as the mean of the 0600–2400 UTC forecasts.

From the DPR instrument, radar reflectivity and rain rate data were regridded to a  $0.1^\circ$  horizontal grid, with the vertical resolution retained at 250 m. Due to its smaller swath width, there were only 12 events (Table 1) during which DPR sampled precipitation in the analysis domain. Simulated reflectivity was computed using the

method of the Thompson et al. (2008) microphysics scheme, assuming a 10-cm radar wavelength. Finally, we regridded model output and DPR data to match the DPR grid, and locations with missing or null data are removed from both datasets, as well as where model output is outside of a DPR swath.

### 3. Results

#### a. Evaluation of GMI-measured water species

Figure 3 shows frequency distributions during OLYMPLEX of simulated and observed water species over the offshore GMI domain in Fig. 2. The model realistically simulated the observed column-integrated water vapor content, with only minor discrepancies between model and observations (Fig. 3a). This result is consistent with Conrick and Mass (2018, manuscript submitted to *J. Hydrometeor.*), who showed that low-level water vapor, wind speed, and IVT from rawinsonde data were accurately forecast during this

TABLE 1. Events during which the GPM DPR instrument passed over the analysis domain in Fig. 2, including an approximate overpass time.

| Overpass times and dates |             |             |
|--------------------------|-------------|-------------|
| 2110 UTC                 | 1625 UTC    | 1310 UTC    |
| 12 Nov 2015              | 30 Nov 2015 | 11 Dec 2015 |
| 1250 UTC                 | 0715 UTC    | 0840 UTC    |
| 14 Nov 2015              | 3 Dec 2015  | 27 Dec 2015 |
| 2100 UTC                 | 1520 UTC    | 2000 UTC    |
| 14 Nov 2015              | 3 Dec 2015  | 11 Jan 2016 |
| 2000 UTC                 | 0610 UTC    | 1740 UTC    |
| 17 Nov 2015              | 8 Dec 2015  | 19 Jan 2016 |

<sup>4</sup> RSS provided the GPM GMI column-integrated values (see <http://www.remss.com/missions/gmi/> for additional details regarding data processing).

<sup>5</sup> For additional information regarding data processing and bias correction, see the NASA documentation ([https://pps.gsfc.nasa.gov/Documents/ATBD\\_GPM\\_V5B\\_April15\\_2018.pdf](https://pps.gsfc.nasa.gov/Documents/ATBD_GPM_V5B_April15_2018.pdf)).

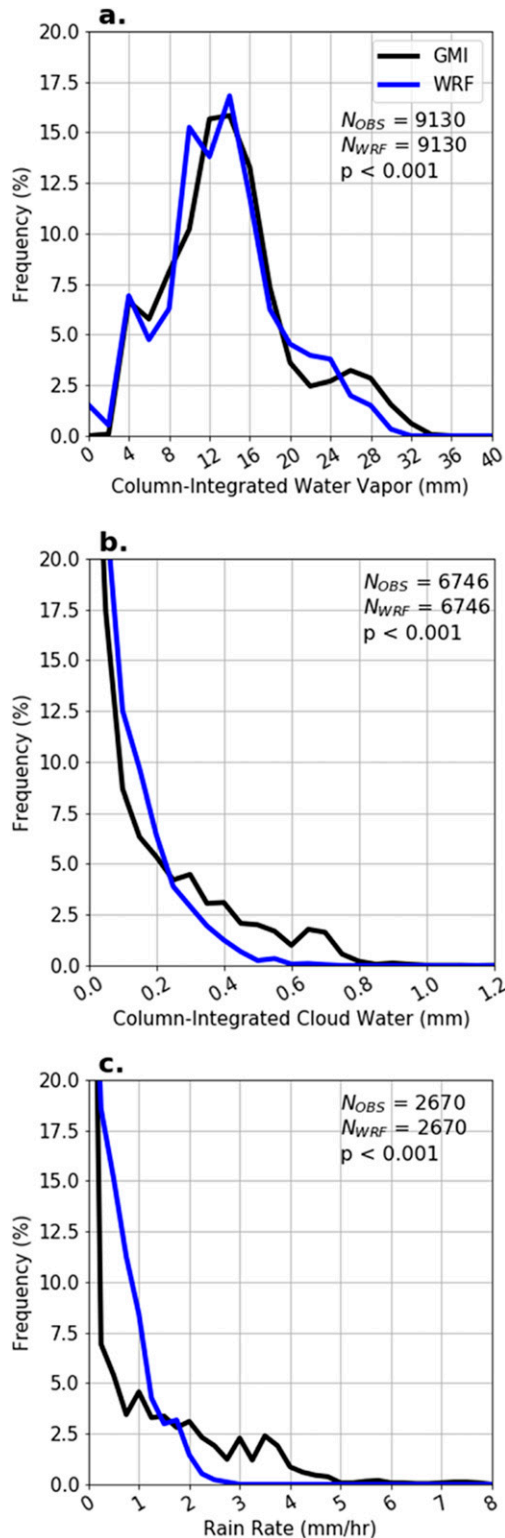


FIG. 3. Observed and simulated frequency distributions of (a) column-integrated water vapor content (mm), (b) column-integrated cloud water content (mm), and (c) surface rain rate ( $\text{mm h}^{-1}$ ) in the GMI domain (Fig. 2). The minimum bin for all panels is 0.0 mm or  $\text{mm h}^{-1}$ , with bin widths for water vapor, cloud water, and rainwater are 2.0 mm, 0.05 mm, and  $0.25 \text{ mm h}^{-1}$ , respectively.

period. Errors were more apparent in the distributions of column-integrated cloud water content and rain rate (Figs. 3b,c). Underprediction was evident in offshore cloud water contents between 0.4 and 0.8 mm, with overprediction at values less than 0.4 mm. The mean bias of cloud water content was  $-0.07 \text{ mm}$  (underprediction). Consistent with cloud water content, WRF rain-rate frequency exceeded observed values for light rain rates below  $1 \text{ mm h}^{-1}$ , while there was considerable underprediction for  $1.5\text{--}6 \text{ mm h}^{-1}$  rain rates. The overall mean precipitation rate from WRF and GMI was  $0.38$  and  $1.22 \text{ mm h}^{-1}$ , respectively, with a mean bias of  $-0.84 \text{ mm h}^{-1}$ . Thus, satellite-based verification of the WRF Model indicate an overall underprediction of rainfall over the ocean during OLYMPEX, which is consistent with the land-based evaluation by Conrick and Mass (2018, manuscript submitted to *J. Hydrometeor.*), which used rain gauges.

To further evaluate whether underpredicted rain rates are related to cloud water deficits, Fig. 4a shows rain-rate error as a function of cloud water error. Low cloud water errors dominate and there is a strong positive correlation ( $r = 0.733$ ) between these data, with an overall tendency toward negative errors (underprediction). In contrast, errors in column-integrated water vapor are only weakly correlated with rain rate ( $r = 0.315$ ; Fig. 4b), with water vapor having less overall bias. These results suggest that the underprediction of simulated rain rates is strongly associated with too little cloud water content in WRF compared to GMI.

To determine whether cloud water content or rain rate was modified as the flow approached land, Fig. 5 shows frequency distributions of simulated and observed (GMI) column-integrated cloud water content (Figs. 5a,b) and rain rate (Figs. 5d,e) at various longitudes. At all longitudes, the underprediction of cloud water content and rain rate is evident when comparing WRF to GMI, except at low cloud water contents and rain rates (Figs. 5c,f). There was minimal upstream orographic enhancement of cloud water content or rain rate in either observations or simulations, with the possible exception of the easternmost longitude ( $124.625^\circ\text{W}$ ) where observations indicate larger values of cloud liquid water (Figs. 5a,d). The small enhancement of cloud liquid water offshore is consistent with the microphysical impact of upstream flow blocking, which can intensify liquid- and ice-phase microphysical processes (Houze and Medina 2005).

#### b. Vertical humidity and hydrometeor profiles

Using rawinsonde observations during OLYMPEX, the vertical distribution of simulated relative humidity (RH) is evaluated to provide an independent verification

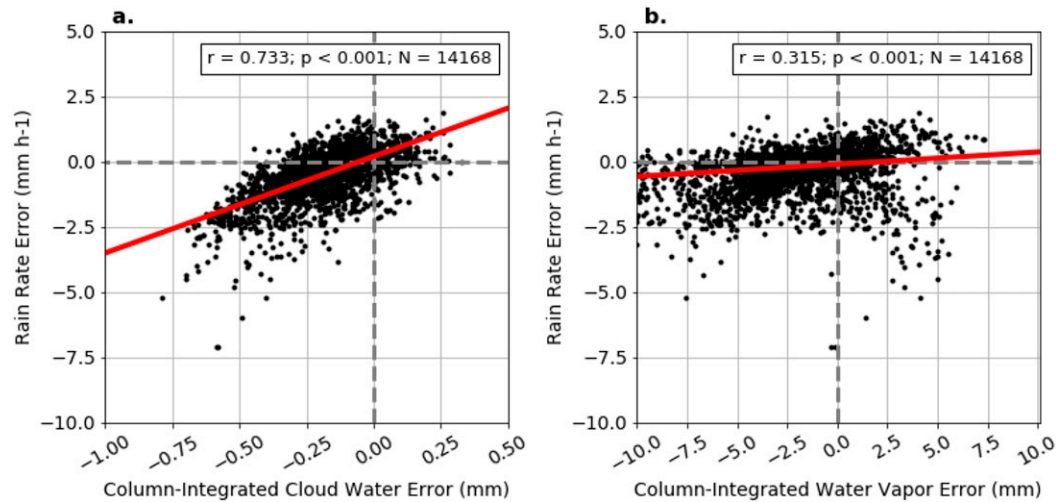


FIG. 4. Scatterplot of (a) column-integrated cloud water content errors (mm) vs rain-rate errors ( $\text{mm h}^{-1}$ ) and (b) column-integrated water vapor errors (mm) vs rain-rate errors ( $\text{mm h}^{-1}$ ) in the GMI domain. The red line indicates the linear regression line and dashed gray lines highlight the origin.

of atmospheric saturation in the model. Rawinsondes were launched by the National Weather Service daily at 0000 and 1200 UTC from Quillayute Airport (UIL) near the Pacific coast on the Olympic Peninsula. Results of this evaluation are shown in Fig. 6 as frequency distributions of RH by height. In both simulations and observations, profiles were generally saturated or nearly saturated below 3 km, with RH decreasing above (Figs. 6a,b). Differences between simulated and observed RH profiles

(Fig. 6c) were minor. Along with IVT (Conrick and Mass 2018, manuscript submitted to *J. Hydrometeor.*) and column-integrated water vapor, the similarity of simulated and observed RH profiles confirms that WRF simulations accurately represented water vapor and the degree of saturation of the incoming flow during OLYMPEX.

Figure 7 shows observed and simulated daily mean vertical profiles of cloud water, rainwater, and snow mixing ratios averaged along various longitudes offshore

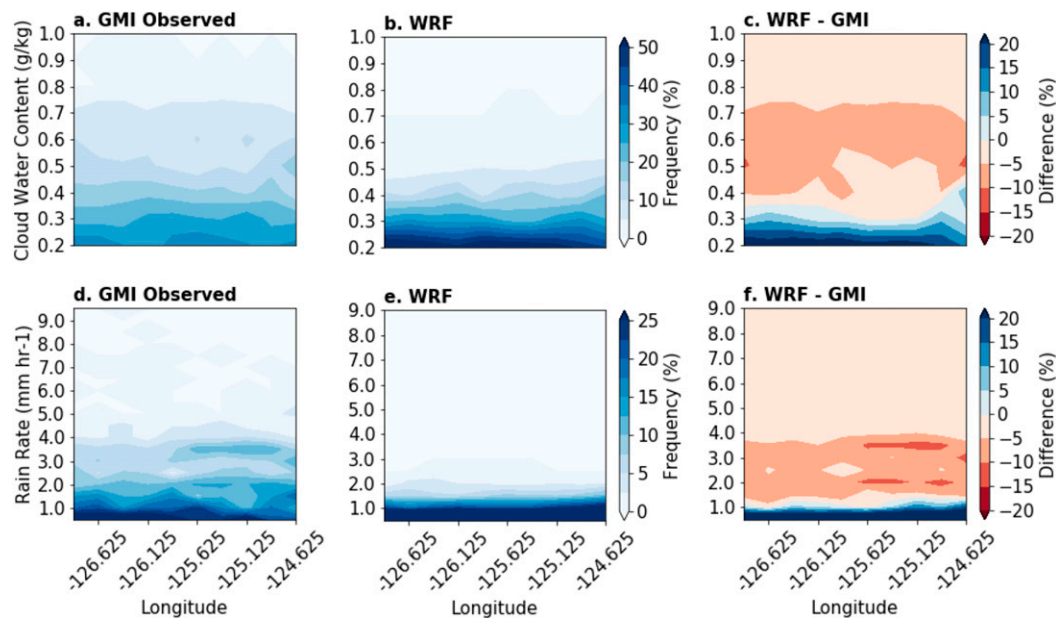


FIG. 5. Frequency distributions of (a)–(c) column-integrated cloud water content and (d)–(f) surface rain rate as a function of longitude for the (a),(d) GMI instrument and (b),(e) UW WRF simulations. (c),(f) The difference between simulated and observed values.

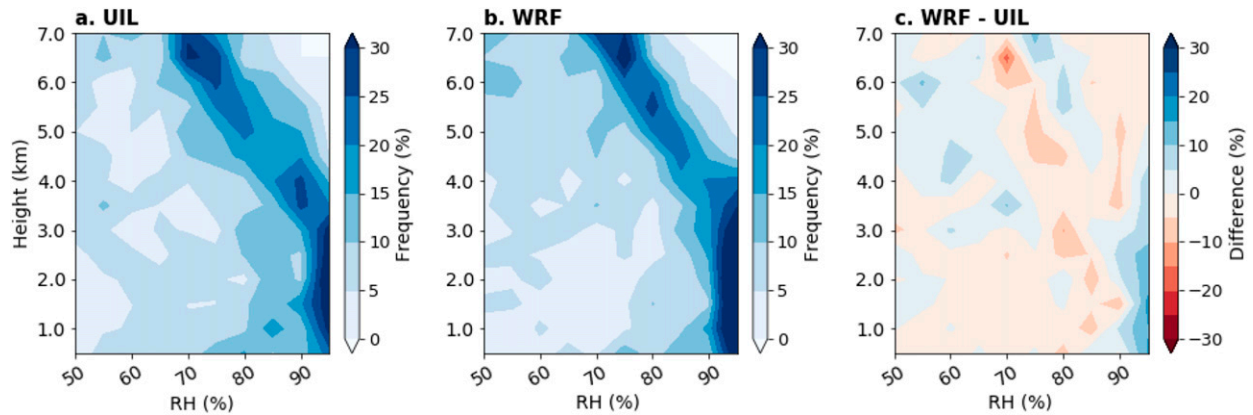


FIG. 6. RH (%) frequencies from (a) rawinsonde observations and (b) the UW WRF as a function of height at the UIL rawinsonde site between 1 Nov 2015 and 1 Feb 2016. (c) The difference between simulated and observed RH at UIL.

of the Washington coast. WRF underpredicted cloud water mixing ratios at 1.25–3 km MSL for all longitudes, with the maximum simulated cloud water content occurring lower than observed: 1.7 versus 2.3 km (Fig. 7a). Directly above the surface, cloud water was overpredicted. Elsewhere in the column, cloud water was realistically simulated. WRF underpredicted rainwater mixing ratios throughout the column (Fig. 7b), in contrast to snow mixing ratios, which the model overpredicted at all levels (Fig. 7c). The maximum quantities of simulated snow mixing ratio occurred at a higher altitude than observed.

Observed mixing ratio profiles varied as a function of longitude. Approaching the coast, GMI indicated a decrease in cloud water, an increase in rainwater, and an increase in snow content. This result agrees with the influence of terrain as described in Stoelinga et al. (2013): vertical motion forced by the barrier increases the rate of conversion from cloud water to hydrometeor species. In contrast, simulated cloud and rainwater profiles experienced little change moving toward the coast, though simulated snow content was enhanced. Additionally, in contrast to GMI observations, the altitude of the simulated snow maximum increased approaching the coast, indicating an increase in cloud depth.

### c. Environmental parameters and model skill

During OLYMPEX, a variety of midlatitude frontal systems impacted the Olympic Peninsula (Houze et al. 2017), with synoptic and mesoscale conditions varying substantially between storm sectors (prefrontal, warm sector, and postfrontal). Because IVT was realistically simulated by the University of Washington (UW) WRF during OLYMPEX (Conrick and Mass 2018, manuscript submitted to *J. Hydrometeor.*), we define storm sectors in terms of IVT as in McMurdie et al. (2018),

using values from the North American Regional Reanalysis (NARR; Mesinger et al. 2006) grid point nearest to the OLYMPEX NASA S-Band Dual Polarimetric (NPOL) radar (Fig. 2). Specifically, we consider the environment to be representative of prefrontal conditions if IVT is between 250 and  $450 \text{ kg m}^{-1} \text{ s}^{-1}$ , representative of postfrontal conditions when IVT is less than  $250 \text{ kg m}^{-1} \text{ s}^{-1}$ , and consistent with a warm-sector environment when IVT exceeds  $450 \text{ kg m}^{-1} \text{ s}^{-1}$ . Prefrontal environments are typically characterized by stable conditions and moderate but increasing melting-level heights, with both ice and liquid microphysics influencing surface precipitation (Zagrodnik et al. 2018). Warm-sector environments are dominated by liquid-phase microphysics, with large IVT and high melting levels. In contrast, ice microphysics are dominant in postfrontal sectors with low melting levels, unstable conditions, and widespread snowfall over higher elevations of the Olympic Mountains (McMurdie et al. 2018). In addition, we evaluated the other environmental parameters used in McMurdie et al. (2018)—925-hPa wind direction and melting-level height—but since results were similar to IVT evaluations they are not described here. Because we consider WRF forecast hours 6–24 and products are averaged daily, errors in timing or location of frontal boundaries will be small.

First, we examine the frequency distributions of observed and simulated rain rate, column-integrated water vapor, and column-integrated cloud water as a function of storm sector (Fig. 8). For all storm sectors, simulated distributions of water vapor contents (Figs. 8a,d,g) were not statistically different from those observed by the GMI instrument, a result consistent with RH profiles and IVT being realistically simulated. For cloud water (Figs. 8b,e,h), the postfrontal sector was most realistically simulated, though some overprediction was present at low values

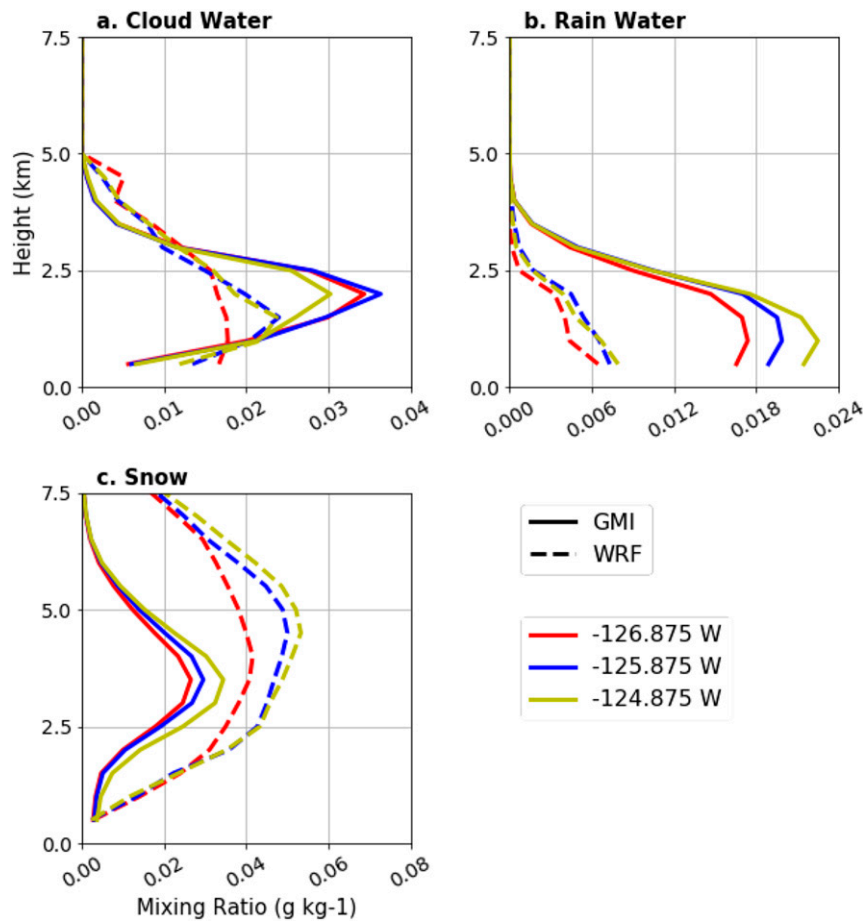


FIG. 7. Daily mean observed (GMI) and simulated (WRF) vertical profiles of (a) cloud water, (b) rainwater, and (c) snow mixing ratios at the longitudes noted in Fig. 2 (yellow:  $\sim 30$  km from the coast; blue:  $\sim 110$  km; red:  $\sim 190$  km).

and underprediction at high values. These biases become larger in the warmer, more moisture-rich prefrontal and warm-sector environments. Rain-rate frequencies (Figs. 8c,f,i) were similar, with postfrontal sectors having the most realistic simulations, though all sectors had an overprediction of light precipitation and underprediction heavier amounts.

Figure 9 shows daily mean vertical profiles of cloud water, rainwater, and snow mixing ratios averaged by storm sector. Postfrontal sectors generally had profiles with the smallest mixing ratios of all sectors. Considering that warm-sector environments are often associated with strong synoptic forcing and large IVT (e.g., Zhu and Newell 1994, Zagrodnik et al. 2018), it was not unexpected that those environments had the greatest mixing ratios among sectors. Compared to GMI, cloud water profiles during pre- and postfrontal conditions were the most realistically simulated (Figs. 9a,g), though cloud water in the warm sectors was as much as 25% smaller in WRF than GMI (Fig. 9d). Rainwater mixing

ratio profiles were underpredicted regardless of environment (Figs. 9b,e,f), with large errors during warm sectors and small errors during prefrontal environments. Finally, simulated snow profiles during warm sectors agreed with GMI at low levels (Fig. 9f), but remained overpredicted elsewhere in the vertical column for all environments (Figs. 9c,i).

#### d. DPR: Reflectivity and rain rates

A subset of 12 DPR overpasses over the DPR region in Fig. 2 were chosen for analysis (Table 1). Because DPR data validity does not depend on surface type, we analyze reflectivity and radar-derived rain rate separately over both land and water to consider model performance with respect to our previous results and orographic effects on precipitation.

Figure 10 displays frequency distributions of rain rates from DPR and WRF over land and ocean. While there is a general overprediction of low rain rates and underprediction of high rain rates, it is of interest to note

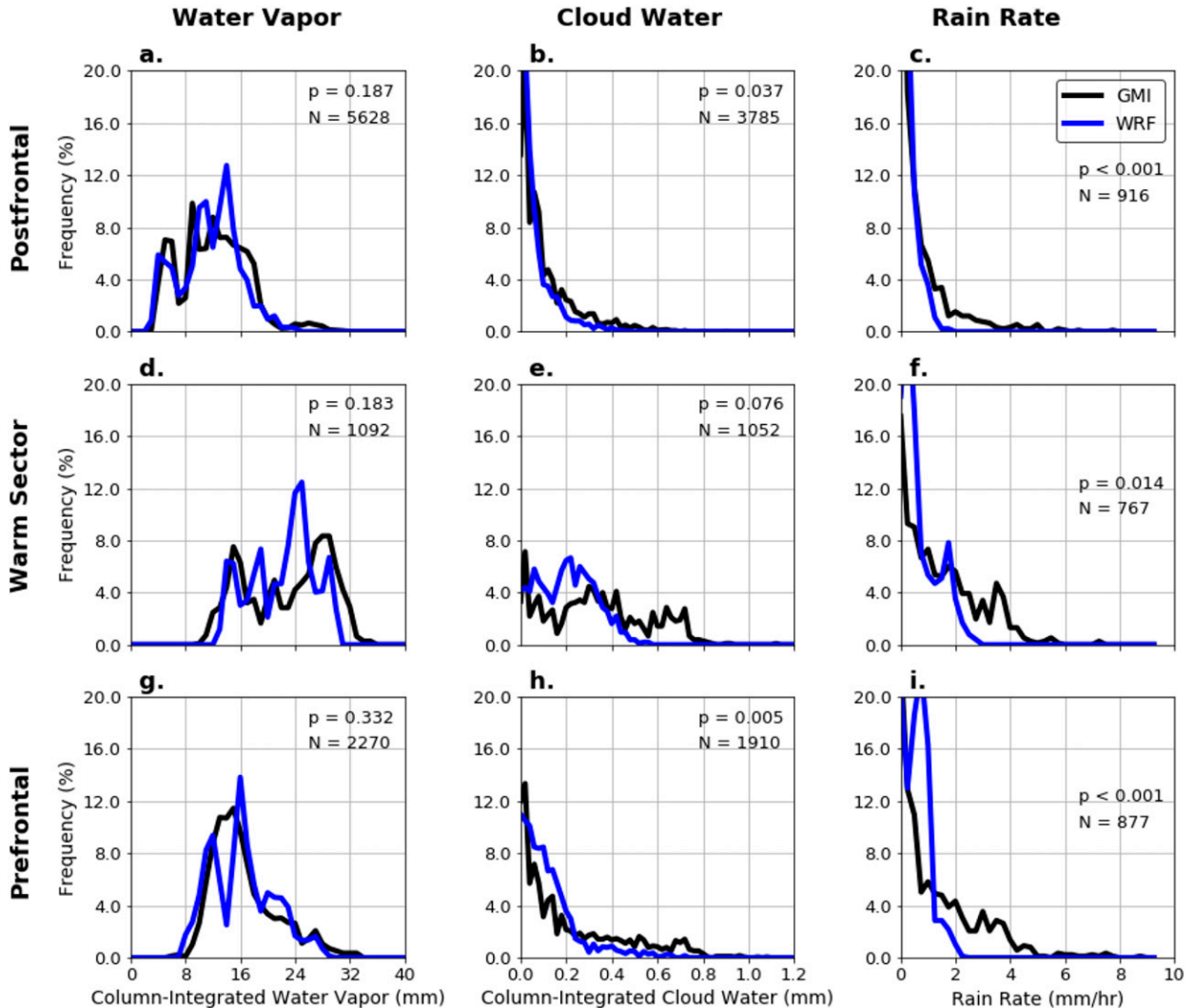


FIG. 8. Frequency distributions as in Fig. 3, except separated by environment based on IVT: (a)–(c) postfrontal, (d)–(f) warm sector, and (g)–(i) prefrontal. The number of events  $N$  in each environment is presented along with the  $p$  value describing whether the two distributions in each panel are statistically different from each other.

that the distribution of rain rates over land is skewed toward larger rates compared to distributions over water. Domain-averaged vertical profiles of simulated and observed radar reflectivity profiles are presented in Fig. 11. At all altitudes, DPR reflectivity values were larger over land than over water, whereas WRF produced generally lower reflectivity over land than over water. Below 2 km, simulated radar reflectivity was underpredicted by as much as 10 dB, with overprediction of a similar magnitude evident above 2 km. From the hydrometeor profiles shown in Fig. 7, we deduce that the excessive simulated snow content relative to GMI is likely responsible for the reflectivity bias above 2 km, whereas the reflectivity deficit below 2 km is the result of too little rainwater in the model.

It is important to note that the DPR retrievals use a wavelength near 2 cm (Ku band), whereas the WRF calculations use a 10-cm wavelength (S band). Therefore, we expect that the observed DPR retrievals would be attenuated to a greater degree by heavy precipitation or large hydrometeors (e.g., Baldini et al. 2012; Battaglia et al. 2015). However, in a study comparing S-band to Ku-band reflectivities, Wen et al. (2011) showed that below 35 dB both wavelengths produce similar reflectivities for a variety of hydrometeor types. Above 35 dB, Ku band tends to be attenuated to a much greater degree in ice than liquid water, the latter of which does not see attenuation until around 45 dB. As a result, it is possible that DPR is underestimating reflectivity in ice-producing regions aloft, though likely not substantially,

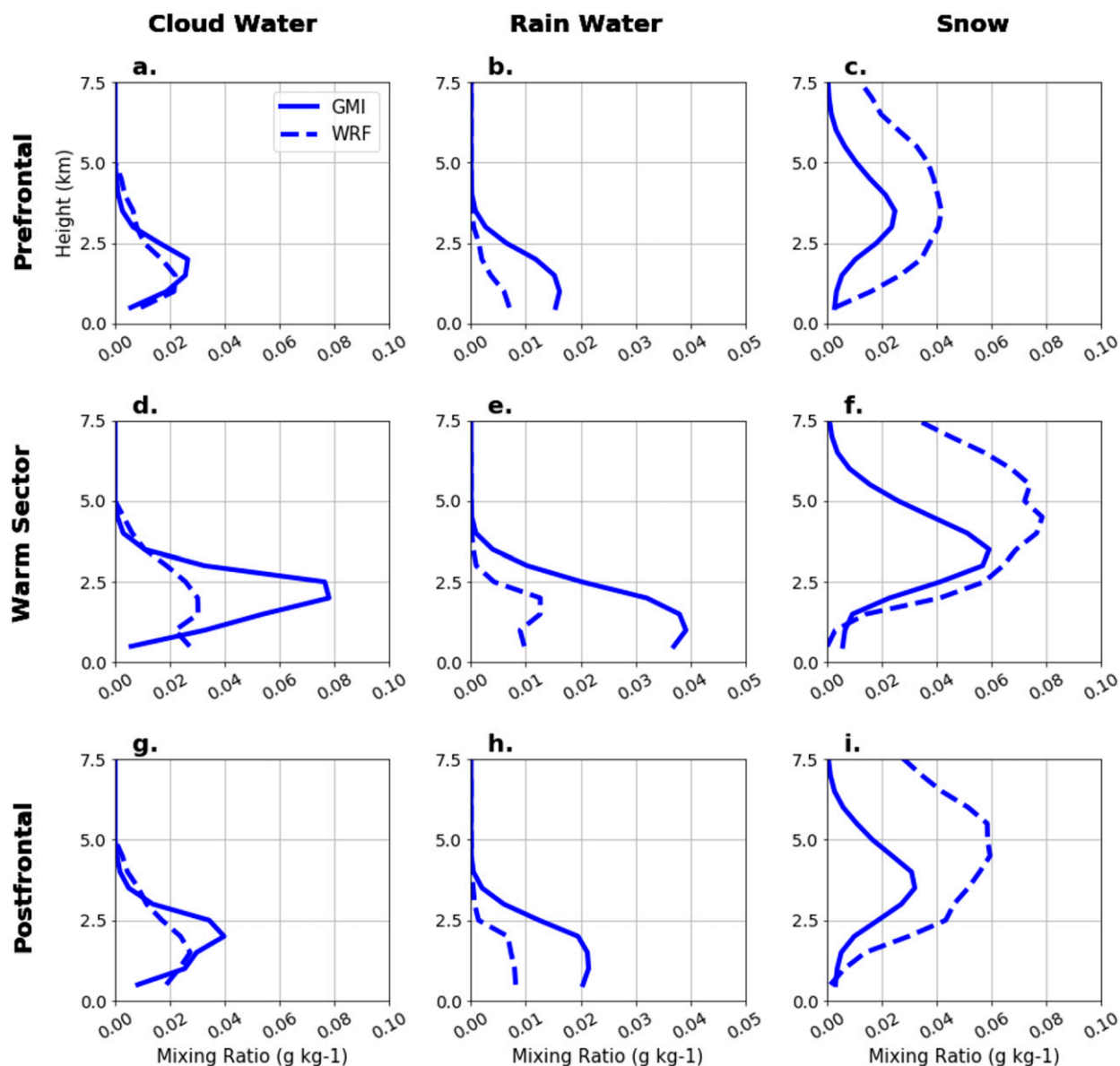


FIG. 9. Daily mean vertical profiles from the GMI instrument (solid) and the UW WRF (dashed) at a central longitude in the GMI domain ( $125.875^{\circ}\text{W}$ ; blue line in Fig. 2,  $\sim 110$  km from the coast). Rows indicate the environment: (a)–(c) prefrontal, (d)–(f) warm sector, and (g)–(i) postfrontal. Columns show different mixing ratios: (left) cloud water, (center) rainwater, and (right) snow.

because the observed mean profiles decrease with altitude and do not exceed 30 dB.

#### 4. Conclusions

The Global Precipitation Measurement (GPM) satellite provides a powerful tool for evaluating moist physics in numerical weather prediction models, particularly over water and complex terrain where observations are difficult to acquire. In this study, we use observations from the GPM Microwave Imager (GMI)

and Dual-Frequency Precipitation Radar (DPR) instruments to evaluate Weather Research and Forecasting (WRF) Model forecasts during the OLYMPEX field campaign using the Thompson et al. (2008) microphysical parameterization. We evaluate a number of aspects of model moist physics, including frequencies of rain rate, column-integrated water vapor and cloud water, vertical profiles of cloud water, rainwater, and snow mixing ratios, and simulated reflectivity.

Results from our evaluation suggest that there are deficiencies in model moist physics over the nearshore

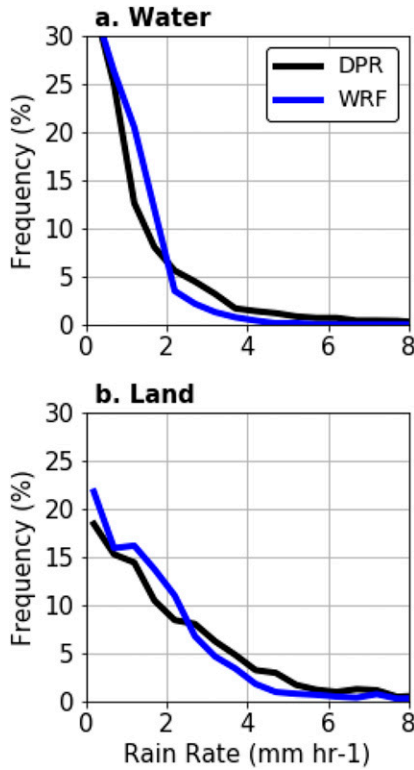


FIG. 10. Frequency distributions of rain rates from DPR and UW WRF as a function of surface type: (a) water and (b) land. Profiles are averaged over the DPR domain in Fig. 2 during the cases in Table 1.

waters and coastal regions of the Pacific Northwest. Consistent with Conrick and Mass (2018, manuscript submitted to *J. Hydrometeor.*) and Laviola et al. (2011), we show that water vapor content was realistically predicted, even though cloud water content and rain rates experienced significant underprediction. Cloud water errors positively correlated with rain-rate errors, suggesting a connection between the underprediction of these quantities.

An evaluation of simulated vertical hydrometeor mixing ratio profiles indicate that WRF underpredicted cloud water from 1.25 to 3 km, underpredicted rainwater at all altitudes, and overpredicted snow throughout the vertical column where temperatures were sufficiently cold. Approaching the Pacific coast from the west, observed cloud water content decreased, while rain and snow contents increased, a result consistent with the influence of upstream topography. WRF struggled to adequately simulate this spatial variation in hydrometeor profiles. For example, in contrast to WRF simulations, DPR profiles had greater reflectivity values over land than water.

Model performance was also evaluated by dividing the analysis period into prefrontal, warm, or postfrontal

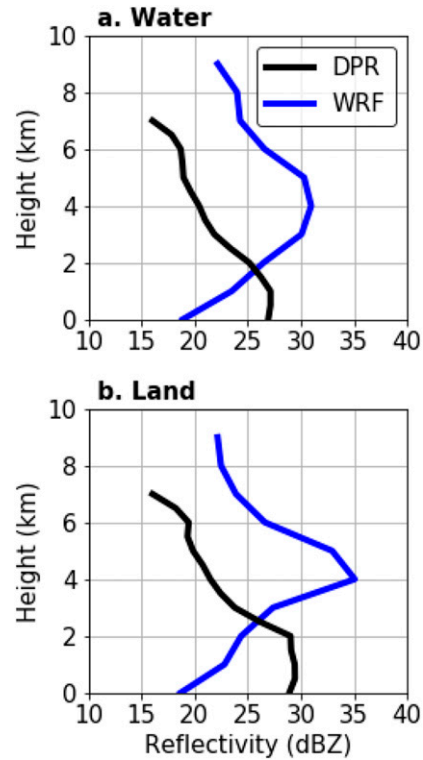


FIG. 11. Domain-averaged vertical profiles of DPR and WRF-simulated radar reflectivity profiles as a function of surface type: (a) water and (b) land. Profiles are averaged over the DPR domain in Fig. 2 during the cases in Table 1.

storm sectors based on integrated vapor transport (IVT), as in McMurdie et al. (2018). Considering frequency distributions and vertical hydrometeor profiles, postfrontal sectors exhibited the greatest degree of agreement between simulations and observations, particularly with respect to cloud water profiles. Warm sectors and prefrontal storm sectors had the greatest errors compared to observations.

Further, since water vapor, cloud water concentrations, and rainfall-rate errors were similar over water and land, it appears that the boundary layer parameterization is not a likely contributor to the microphysical biases we described. Thus, with the incoming atmospheric water vapor content and saturation profiles accurately represented in the simulations, and similar biases noted for widely varying environmental conditions and surface characteristics, it appears that significant microphysical problems exist in the modeling system.

An outstanding question is the origin of these deficiencies: Are they due to deficient warm-rain processes, ice-phase microphysics, or the processes that connect them? Our results show the pervasive underprediction of rain and cloud water, coupled with the

overprediction of snow aloft. Poor representation of warm-rain process could cause errors in, for example, the generation of and conversion from cloud water to rain in the model, which may lead to the underprediction of these quantities. Deficient ice microphysics in the model, on the other hand, may explain the overprediction of snow aloft, preventing sufficient seeding of low-level precipitation. Our future work will focus on evaluating the origin of these existing biases and how they can be corrected.

*Acknowledgments.* This work was supported by the National Science Foundation through Grant AGS-1349847. The authors thank Dr. Greg Thompson, Dr. Hugh Morrison, Dr. Robert Houze, and Joseph Zagrodnik for their comments and insight. We also acknowledge Stacy Brodzik for data and technical support. The authors thank three anonymous reviewers for valuable suggestions that resulted in significant improvements to the manuscript.

#### REFERENCES

- Baldini, L., V. Chandrasekar, and D. Moisseev, 2012: Microwave radar signatures of precipitation from S band to Ka band: Application to GPM mission. *Eur. J. Remote Sens.*, **45**, 75–88, <https://doi.org/10.5721/EuJRS20124508>.
- Barros, A., 2013: Orographic precipitation, freshwater resources, and climate vulnerabilities in mountainous regions. *Climate Vulnerability: Understanding and Addressing Threats to Essential Resources*, Academic Press, 57–78.
- Battaglia, A., S. Tanelli, K. Mroz, and F. Tridon, 2015: Multiple scattering in observations of the GPM Dual-Frequency Precipitation Radar: Evidence and impact on retrievals. *J. Geophys. Res. Atmos.*, **120**, 4090–4101, <https://doi.org/10.1002/2014JD022866>.
- Bikos, D., and Coauthors, 2012: Synthetic satellite imagery for real-time high-resolution model evaluation. *Wea. Forecasting*, **27**, 784–795, <https://doi.org/10.1175/WAF-D-11-00130.1>.
- Bodas-Salcedo, A., K. D. Williams, P. R. Field, and A. P. Lock, 2012: The surface downwelling solar radiation surplus over the Southern Ocean in the Met Office model: The role of midlatitude cyclone clouds. *J. Climate*, **25**, 7467–7486, <https://doi.org/10.1175/JCLI-D-11-00702.1>.
- Chaboureaud, J.-P., J.-P. Cammas, P. J. Mascart, J.-P. Pinty, and J.-P. Lafore, 2002: Mesoscale model cloud scheme assessment using satellite observations. *J. Geophys. Res.*, **107**, 4301, <https://doi.org/10.1029/2001JD000714>.
- Field, P. R., R. J. Hogan, P. R. A. Brown, A. J. Illingworth, T. W. Choullarton, and R. J. Cotton, 2005: Parameterization of ice-particle size distributions for mid-latitude stratiform cloud. *Quart. J. Roy. Meteor. Soc.*, **131**, 1997–2017, <https://doi.org/10.1256/qj.04.134>.
- Gao, J., G. Tang, and Y. Hong, 2017: Similarities and improvements of GPM Dual-Frequency Precipitation Radar (DPR) upon TRMM Precipitation Radar (PR) in global precipitation rate estimation, type classification and vertical profiling. *Remote Sens.*, **9**, 1142, <https://doi.org/10.3390/rs911142>.
- Garand, L., and S. Nadon, 1998: High-resolution satellite analysis and model evaluation of clouds and radiation over the Mackenzie Basin using AVHRR data. *J. Climate*, **11**, 1976–1996, <https://doi.org/10.1175/1520-0442-11.8.1976>.
- Grell, G. A., and S. R. Freitas, 2014: A scale and aerosol aware stochastic convective parameterization for weather and air quality modeling. *Atmos. Chem. Phys.*, **14**, 5233–5250, <https://doi.org/10.5194/acp-14-5233-2014>.
- Hong, S. Y., Y. Noh, and J. Dudhia, 2006: A new vertical diffusion package with an explicit treatment of entrainment processes. *Mon. Wea. Rev.*, **134**, 2318–2341, <https://doi.org/10.1175/MWR3199.1>.
- Hou, A. Y., and Coauthors, 2014: The Global Precipitation Measurement Mission. *Bull. Amer. Meteor. Soc.*, **95**, 701–722, <https://doi.org/10.1175/BAMS-D-13-00164.1>.
- Houze, R. A., Jr., and S. Medina, 2005: Turbulence as a mechanism for orographic precipitation enhancement. *J. Atmos. Sci.*, **62**, 3599–3623, <https://doi.org/10.1175/JAS3555.1>.
- , and Coauthors, 2017: The Olympic Mountains Experiment (OLYMPEX). *Bull. Amer. Meteor. Soc.*, **98**, 2167–2188, <https://doi.org/10.1175/BAMS-D-16-0182.1>.
- Huang, Y., S. T. Siems, M. J. Manton, and G. Thompson, 2014: An evaluation of WRF simulations of clouds over the Southern Ocean with A-Train observations. *Mon. Wea. Rev.*, **142**, 647–667, <https://doi.org/10.1175/MWR-D-13-00128.1>.
- Iacono, M. J., J. S. Delamere, E. J. Mlawer, M. W. Shephard, S. A. Clough, and W. D. Collins, 2008: Radiative forcing by long-lived greenhouse gases: Calculations with the AER radiative transfer models. *J. Geophys. Res.*, **113**, D13103, <https://doi.org/10.1029/2008JD009944>.
- Iguchi, T., and R. Meneghini, 2016a: GPM GMI (GPROF) radiometer precipitation profiling L3 1 day 0.25 degree × 0.25 degree, version 05. Goddard Earth Sciences Data and Information Services Center, accessed 1 July 2018, <https://doi.org/10.5067/GPM/GMI/3A-DA/05>.
- , and —, 2016b: GPM DPR Ku precipitation profile 2A 1.5 hours 5 km, version 05. Goddard Earth Sciences Data and Information Services Center, accessed 1 July 2018, <https://doi.org/10.5067/GPM/DPR/KU/2A/05>.
- Jankov, I., and Coauthors, 2011: An evaluation of five ARW-WRF microphysics schemes using synthetic GOES imagery for an atmospheric river event affecting the California coast. *J. Hydrometeorol.*, **12**, 618–633, <https://doi.org/10.1175/2010JHM1282.1>.
- Keil, C., A. Taffermer, H. Mannstein, and U. Schättler, 2003: Evaluating high-resolution model forecasts of European winter storms by use of satellite and radar observations. *Wea. Forecasting*, **18**, 732–747, [https://doi.org/10.1175/1520-0434\(2003\)018<0732:EHMFOE>2.0.CO;2](https://doi.org/10.1175/1520-0434(2003)018<0732:EHMFOE>2.0.CO;2).
- Kim, J., D. Shin, and C. Kummerow, 2013: Impacts of a priori databases using six WRF microphysics schemes on passive microwave rainfall retrievals. *J. Atmos. Oceanic Technol.*, **30**, 2367–2381, <https://doi.org/10.1175/JTECH-D-12-00261.1>.
- Kubota, T., and Coauthors, 2014: Evaluation of precipitation estimates by at-launch codes of GPM/DPR algorithms using synthetic data from TRMM/PR observations. *IEEE J. Sel. Top. Appl. Earth Obs. Remote Sens.*, **7**, 3931–3944, <https://doi.org/10.1109/JSTARS.2014.2320960>.
- Kummerow, C., W. Barnes, T. Kozu, J. Shiue, and J. Simpson, 1998: The Tropical Rainfall Measuring Mission (TRMM) sensor package. *J. Atmos. Oceanic Technol.*, **15**, 809–817, [https://doi.org/10.1175/1520-0426\(1998\)015<0809:TTRMMT>2.0.CO;2](https://doi.org/10.1175/1520-0426(1998)015<0809:TTRMMT>2.0.CO;2).

- Laviola, S., A. Moscatello, M. M. Miglietta, E. Cattani, and V. Levizzani, 2011: Satellite and numerical model investigation of two heavy rain events over the central Mediterranean. *J. Hydrometeorol.*, **12**, 634–649, <https://doi.org/10.1175/2011JHM1257.1>.
- Ma, Y., G. Tang, D. Long, B. Yong, L. Zhong, W. Wan, and Y. Hong, 2016: Similarity and error intercomparison of the GPM and its predecessor-TRMM multisatellite precipitation analysis using the best available hourly gauge network over the Tibetan Plateau. *Remote Sens.*, **8**, 569, <https://doi.org/10.3390/rs8070569>.
- McMurdie, L. A., A. K. Rowe, R. A. Houze Jr., S. R. Brodzik, J. P. Zagrodnik, and T. M. Schuldt, 2018: Terrain-enhanced precipitation processes above the melting layer: Results from OLYMPEX. *J. Geophys. Res. Atmos.*, **123**, 12 194–12 209, <https://doi.org/10.1029/2018JD029161>.
- Mesinger, F. G., and Coauthors, 2006: North American Regional Reanalysis. *Bull. Amer. Meteor. Soc.*, **87**, 343–360, <https://doi.org/10.1175/BAMS-87-3-343>.
- Niu, G.-Y., and Coauthors, 2011: The community Noah land surface model with multiparameterization options (Noah-MP): 1. Model description and evaluation with local-scale measurements. *J. Geophys. Res.*, **116**, D12109, <https://doi.org/10.1029/2010JD015139>.
- Otkin, J. A., and T. J. Greenwald, 2008: Comparison of WRF model-simulated and MODIS-derived cloud data. *Mon. Wea. Rev.*, **136**, 1957–1970, <https://doi.org/10.1175/2007MWR2293.1>.
- Rakesh, V., R. Singh, P. K. Pal, and P. C. Joshi, 2009: Impacts of satellite-observed winds and total precipitable water on WRF short-range forecasts over the Indian region during the 2006 summer monsoon. *Wea. Forecasting*, **24**, 1706–1731, <https://doi.org/10.1175/2009WAF2222242.1>.
- Shi, J. J., and Coauthors, 2010: WRF simulations of the 20–22 January 2007 snow events over eastern Canada: Comparison with in situ and satellite observations. *J. Appl. Meteor. Climatol.*, **49**, 2246–2266, <https://doi.org/10.1175/2010JAMC2282.1>.
- Skamarock, W. C., and Coauthors, 2008: A description of the Advanced Research WRF version 3. NCAR Tech. Note NCAR/TN-475+STR, 113 pp., <https://doi.org/10.5065/D68S4MVH>.
- Skofronick-Jackson, G., and Coauthors, 2017: The Global Precipitation Measurement (GPM) Mission for science and society. *Bull. Amer. Meteor. Soc.*, **98**, 1679–1695, <https://doi.org/10.1175/BAMS-D-15-00306.1>.
- Speirs, P., M. Gabella, and A. Berne, 2017: A comparison between the GPM Dual-Frequency Precipitation Radar and ground-based radar precipitation rate estimates in the Swiss Alps and Plateau. *J. Hydrometeorol.*, **18**, 1247–1269, <https://doi.org/10.1175/JHM-D-16-0085.1>.
- Stephens, G. L., and Coauthors, 2002: The *CloudSat* mission and the A-Train: A new dimension of space-based observations of clouds and precipitation. *Bull. Amer. Meteor. Soc.*, **83**, 1771–1790, <https://doi.org/10.1175/BAMS-83-12-1771>.
- Stoelinga, M. T., R. E. Stewart, G. Thompson, and J. M. Thériault, 2013: Microphysical processes within winter orographic cloud and precipitation systems. *Mountain Weather Research and Forecasting*, F. K. Chow, S. F. J. de Wekker, and B. J. Snyder, Eds., Springer, 345–408.
- Sun, Z., and L. Rikus, 2004: Validating model clouds and their optical properties using geostationary satellite imagery. *Mon. Wea. Rev.*, **132**, 2006–2020, [https://doi.org/10.1175/1520-0493\(2004\)132<2006:VMCATO>2.0.CO;2](https://doi.org/10.1175/1520-0493(2004)132<2006:VMCATO>2.0.CO;2).
- Thompson, G., P. R. Field, R. M. Rasmussen, and W. D. Hall, 2008: Explicit forecasts of winter precipitation using an improved bulk microphysics scheme. Part II: Implementation of a new snow parameterization. *Mon. Wea. Rev.*, **136**, 5095–5115, <https://doi.org/10.1175/2008MWR2387.1>.
- Tian, F., S. Hou, L. Yang, H. Hu, and A. Hou, 2018: How does the evaluation of the GPM IMERG rainfall product depend on gauge density and rainfall intensity? *J. Hydrometeorol.*, **19**, 339–349, <https://doi.org/10.1175/JHM-D-17-0161.1>.
- Vasić, S., C. A. Lin, I. Zawadzki, O. Bousquet, and D. Chaumont, 2007: Evaluation of precipitation from numerical weather prediction models and satellites using values retrieved from radars. *Mon. Wea. Rev.*, **135**, 3750–3766, <https://doi.org/10.1175/2007MWR1955.1>.
- Wen, Y., Y. Hong, G. Zhang, T. J. Schuur, J. J. Gourley, Z. Flamig, K. R. Morris, and Q. Cao, 2011: Cross validation of spaceborne radar and ground polarimetric radar aided by polarimetric echo classification of hydrometeor types. *J. Appl. Meteor. Climatol.*, **50**, 1389–1402, <https://doi.org/10.1175/2011JAMC2622.1>.
- Wentz, F. J., T. Meissner, J. Scott, and K. A. Hilburn, 2015: Remote Sensing Systems GPM GMI environmental suite on 0.25 deg grid, version 8.2. Remote Sensing Systems, accessed 1 July 2018, [www.remss.com/missions/gmi](http://www.remss.com/missions/gmi).
- Zagrodnik, J. P., L. A. McMurdie, and R. A. Houze Jr., 2018: Stratiform precipitation processes in cyclones passing over a coastal mountain range. *J. Atmos. Sci.*, **75**, 983–1004, <https://doi.org/10.1175/JAS-D-17-0168.1>.
- Zhang, X., E. N. Anagnostou, M. Frediani, S. Solomos, and G. Kallos, 2013: Using NWP simulations in satellite rainfall estimation of heavy precipitation events over mountainous areas. *J. Hydrometeorol.*, **14**, 1844–1858, <https://doi.org/10.1175/JHM-D-12-0174.1>.
- Zhu, Y., and R. E. Newell, 1994: Atmospheric rivers and bombs. *Geophys. Res. Lett.*, **21**, 1999–2002, <https://doi.org/10.1029/94GL01710>.